Check for updates

Solar RRL

RESEARCH ARTICLE OPEN ACCESS

Plasma-Enhanced Chemical Vapor Deposition-Grown Zinc Oxide Thin Films for Silicon Heterojunction Solar Cells

Muhammad Ainul Yaqin[1,2] | Alexander Eberst[1] | Alexandr Zamchiy[1] | Felix Gunkel[3] | Andreas Lambertz[1] | Karsten Bittkau[1] | Alexandros Sarantopoulos[3] | Uwe Rau[1,2] | Kaining Ding[1]

[1]IMD-3: Photovoltaics, Forschungszentrum Jülich GmbH, Jülich, Germany | [2]Jülich-Aachen Research Alliance (JARA-Energy) and Faculty of Electrical Engineering and Information Technology, RWTH Aachen University, Aachen, Germany | [3]Peter Grünberg Institute-Electronic Materials (PGI-7), Forschungszentrum Jülich GmbH, Jülich, Germany

Correspondence: Muhammad Ainul Yaqin (m.yaqin@fz-juelich.de) | Kaining Ding (k.ding@fz-juelich.de)

Received: 30 January 2026 | **Revised:** 11 May 2026 | **Accepted:** 1 July 2026

Keywords: plasma-enhanced chemical vapor deposition | silicon heterojunction solar cells | transparent conductive oxides | zinc oxide

ABSTRACT

Zinc oxide thin films are successfully deposited using plasma-enhanced chemical vapor deposition (PECVD), representing a novel approach for fabricating transparent conductive oxide (TCO) layers. The initial undoped ZnO film exhibits a polycrystalline structure with a pronounced (002) orientation and low optical absorptance. However, the electrical properties of the film are characterized by high resistivity and instability, primarily attributed to its porous morphology. These limitations can be addressed by incorporating aluminum-doped zinc oxide or indium tin oxide seed layers, resulting in enhanced and more stable electrical performance. To demonstrate its applicability, this study reports the first successful integration of PECVD-grown ZnO film as a front-contact layer in silicon heterojunction solar cells. The addition of seed layers boosts the solar cell efficiency by increasing the fill factor through reduced series resistance. Despite the challenges with the initial film quality and the need to further refine the PECVD conditions to optimize the device performance, this study offers valuable insights into the current limitations and future potential of PECVD for TCO development. This lays the foundation for improving the PECVD process to produce high-quality TCO, potentially establishing it as an alternative deposition method for next-generation photovoltaic technology.

1 | Introduction

Silicon heterojunction (SHJ) solar cells represent a promising advancement in crystalline silicon solar cell technology for future photovoltaic (PV) applications [1]. These cells, equipped with an intrinsic amorphous silicon passivation layer, can achieve a high open-circuit voltage (V_{OC}) exceeding 750 mV, coupled with an excellent fill factor (FF) [2]. A record-breaking power conversion efficiency (PCE) of 26.81% was achieved by LONGi through the incorporation of nanocrystalline silicon passivating contact layers and optimization of both front and rear optics [3]. In addition to remarkable PCE, SHJ technology offers several advantages for mass production in PV, including better temperature coefficient, low manufacturing temperatures, and the utilization of thin silicon wafers [4–6]. However, the low conductivity of amorphous and nanocrystalline silicon layer hinders the efficient collection of charge carriers by the electrodes. Consequently, transparent conductive oxides (TCO) are essential in SHJ solar cells, serving as the contact layers to facilitate efficient carrier collection while maintaining high optical transparency [7, 8]. An ideal TCO for SHJ applications must combine high electrical conductivity with excellent transparency across the visible spectrum to minimize electrical and optical losses [9, 10]. Magnetron sputtering remains the predominant method for TCO fabrication due to its high deposition rate and industrial scalability [9]. Nonetheless, alternative deposition techniques, such as atomic layer deposition, rapid plasma deposition, and pulsed laser deposition, have been explored to enhance film performance and

This is an open access article under the terms of the Creative Commons Attribution License, which permits use, distribution and reproduction in any medium, provided the original work is properly cited.

© 2026 The Author(s). *Solar RRL* published by Wiley-VCH GmbH.

processing flexibility [11–14]. Among various thin-film deposition techniques, plasma-enhanced chemical vapor deposition (PECVD) remains underexplored for direct TCO deposition, despite its potential advantages including excellent control over dopant incorporation for tunable film properties [15].

Currently, the predominant sputtered TCO films are composed of indium-based materials such as indium tin oxide (ITO), indium zinc oxide (IZO), and Zr-doped indium oxide [14, 16–18]. However, owing to the limited availability and high cost of indium resources, coupled with growing environmental and sustainability concerns, there has been progressive development of indium-saving TCO films [19]. These include ZnO- and SnO_x-based thin films [20–22]. ZnO is considered a promising TCO material due to its natural abundance and favorable optical and electrical properties [23]. ZnO films have been proposed as substitutes for indium-based TCO in SHJ solar cells, particularly when doped with elements such as boron (B), aluminum (Al), or gallium (Ga) [24–26].

In this study, we develop ZnO films deposited using a PECVD system and investigate the fundamental properties of these films, focusing on their electrical, optical, and microstructural characteristics. Sputtered aluminum-doped zinc oxide (AZO) was used as a reference to benchmark the performance of the PECVD-grown films. Our initial findings indicate that the PECVD-deposited ZnO films exhibit inferior performance compared to the reference AZO, particularly in terms of their resistivity. To address this limitation, we explored the use of seed layers to enhance the film properties. Additionally, we demonstrate the direct application of PECVD undoped ZnO on SHJ solar cells. Although the current PECVD process underperforms in terms of cell performance, the present results could lead to further investigations into PECVD TCO.

2 | Results and Discussion

2.1 | Properties of Undoped ZnO Thin Films

Table 1 summarizes the charge carrier concentration (n), charge carrier mobility (μ), and resistivity (ρ) of both the undoped ZnO film and the sputter-deposited AZO, as determined through Hall measurements using the van der Pauw method. It is well known that undoped ZnO demonstrates n-type conductivity, which is attributed to intrinsic defects such as oxygen vacancies (V_o) and Zn interstitials (Zn_i) [27, 28]. Our undoped ZnO film exhibited a charge carrier concentration exceeding 10^{20} cm^{-3}, similar to that of a typical TCO [9]. However, a significant difference emerged in the charge carrier mobility; the undoped ZnO film showed a low mobility of 2.3 cm^2/Vs, which is substantially lower than 17.1 cm^2/Vs measured for the reference sputtered AZO. Note that both films have similar thickness of ≈100 nm.

TABLE 1 | Charge carrier concentration, charge carrier mobility, and resistivity of PECVD undoped ZnO and reference sputter AZO.

	n, 10^{20} cm^{-3}	μ, cm^2/Vs	ρ, 10^{-3} Ω·cm
Undoped ZnO	1.5	2.3	16
Sputter AZO	2.0	17.1	1.8

It is known that the resistivity of film is governed by both n and μ which is shown in the following formula

$$\rho = \frac{1}{\mu n q}$$

This poor mobility observed in the undoped ZnO film translates directly into a resistivity that is an order of magnitude higher than that of the reference AZO. The substantial difference in electrical performance highlights the immediate need to prioritize the enhancement of charge carrier mobility in the ongoing development of undoped ZnO film via PECVD process.

In addition to electrical properties, optical properties are a primary characteristic for evaluating the TCO layer. As shown in Figure 1, the optical transmittance and absorptance are depicted within the wavelength range from 300 to 1300 nm. The undoped ZnO film exhibited high optical transmittance exceeding 80% with low absorptance, comparable to that of the reference AZO film. Further ellipsometer measurements provided insight into the density of the material via the refractive index. As a material becomes denser, the light interacts more with its atoms, causing the light to slow down, thus resulting higher refractive index. The refractive index of the undoped ZnO film was consistently lower than that of the AZO reference across the entire measured spectral range. A refractive index in the 1.9–2.1 range is generally considered indicative of a high-quality film whose microstructure closely resembles dense, well-performed AZO [29]. The deviation in the refractive index usually indicates the presence of porosity in the undoped ZnO film [30]. By applying Maxwell–Garnett effective medium approximation (EMA) from ellipsometer, where a reference sputtered AZO is used as a model for dense ZnO, further analysis revealed that the undoped ZnO film has a void fraction of 16.4%, explicitly confirming a certain degree of porosity. This is further substantiated by X-ray reflectivity (XRR) analysis shown in Figure S1 and Table S1, which determined the density of the undoped ZnO film to be 5.27 g/cm^3, which is lower than the 5.54 g/cm^3 measured for the sputtered AZO.

The refractive index and density information provided significant motivation for a detailed examination of the surface morphology of the films using scanning electron microscopy (SEM), atomic force microscopy (AFM), and contact angle measurements, as shown in Figure 2. The SEM images in top-view showed morphology of undoped ZnO film, revealing an irregular shape characterized by discontinuities and distinct voids between grains, a feature previously noted in another PECVD ZnO study [31]. This less dense structure differs significantly from that of reference sputtered AZO, which possesses larger and denser grains. Importantly, the presence of these voids and grain boundary discontinuities is expected to act as charge carrier scattering sites, providing a plausible explanation for the poor charge carrier mobility observed in the undoped ZnO film [32]. Further structural assessments confirmed the morphological distinctions; the undoped ZnO film exhibited a higher root mean square roughness of 4.3 nm, compared to 1.7 nm for the sputtered AZO. This rougher morphology also impacted the film surface energy,

2367198x, 2026, 14, Downloaded from https://onlinelibrary.wiley.com/doi/10.1002/solr.70431 by Universitatsbibliothek RWTH Aachen University, Wiley Online Library on [03/08/2026]. See the Terms and Conditions (https://onlinelibrary.wiley.com/terms-and-conditions) on Wiley Online Library for rules of use; OA articles are governed by the applicable Creative Commons License

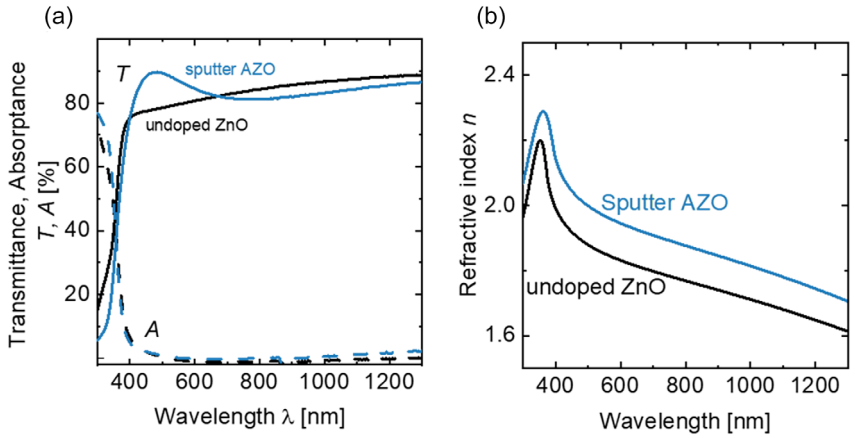


FIGURE 1 | Optical properties of undoped ZnO and sputter AZO thin films on glass substrate. (a) Spectral transmittance and absorptance measured in the wavelength range from 300 to 1300 nm using UV–Vis–NIR spectroscopy. (b) Refractive index extracted from spectroscopic ellipsometry.

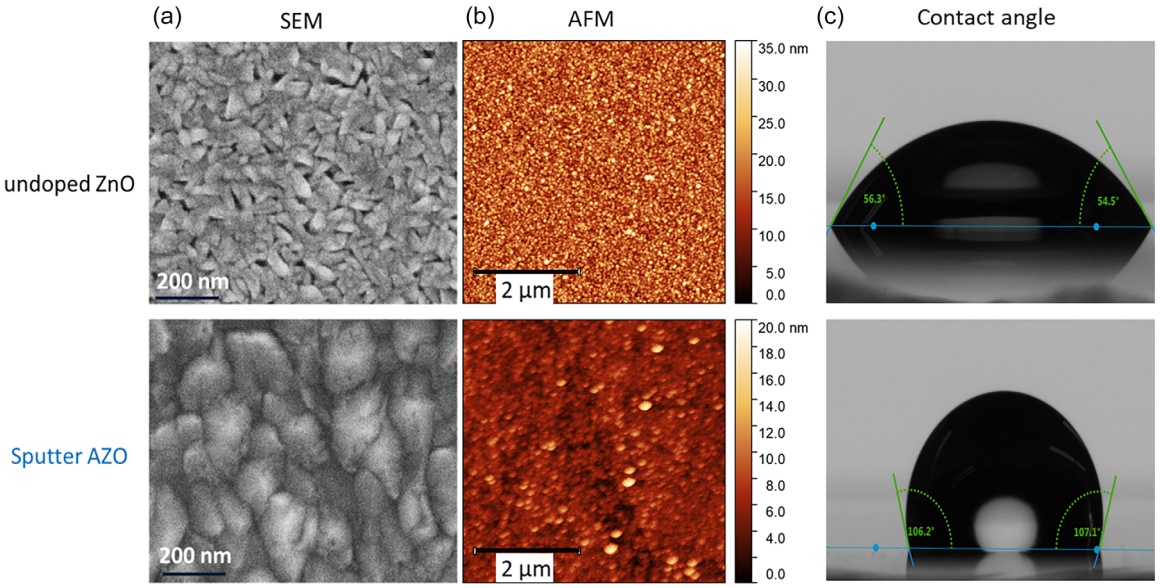


FIGURE 2 | Surface morphology and wettability of undoped ZnO and sputter AZO thin films. (a) Top-view SEM images showing grain structure. (b) Atomic force microscope surface topography used to determine surface roughness. (c) Contact angle measurements indicating surface wettability.

leading to hydrophilic characteristics (contact angle of 54°–56°), in contrast to the hydrophobic sputtered AZO (contact angle of 106°–107°). We hypothesize that the combined high surface roughness and internal porosity facilitate water molecules penetration, resulting in undesirable hydrophilic behavior where potential moisture-induced degradation is a concern for solar cell applications [33].

Grazing incidence X-ray diffraction (GIXRD) was employed to examine the crystal structure, as shown in Figure 3. Both films exhibited diffraction peaks that could be indexed to the hexagonal wurtzite structure according to JCPDS 36-1451. The PECVD undoped ZnO film demonstrated a strong (002) diffraction peak, alongside smaller (100) and (101) peaks, indicating a polycrystalline structure with a highly preferred *c*-axis orientation, a characteristic frequently reported for ZnO films grown via chemical vapor deposition (CVD) [32, 34, 35]. Furthermore, no impurity peaks were detected, confirming high phase purity. However, the (002) peak intensity was lower than that of sputtered

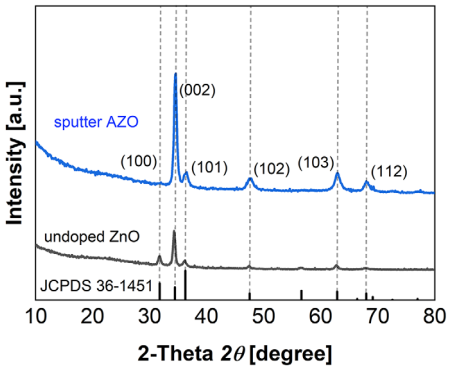


FIGURE 3 | XRD patterns of undoped ZnO and sputter AZO thin films with JCPDS 36-1451 reference.

AZO, suggesting a lower degree of crystallinity in the undoped ZnO film [36, 37]. The mean crystallite sizes, calculated from the full width at half maximum (FWHM) of (002) peak using

2367198x, 2026, 14, Downloaded from https://onlinelibrary.wiley.com/doi/10.1002/solr.70431 by Universitatsbibliothek RWTH Aachen University, Wiley Online Library on [03/08/2026]. See the Terms and Conditions (https://onlinelibrary.wiley.com/terms-and-conditions) on Wiley Online Library for rules of use; OA articles are governed by the applicable Creative Commons License

Debye–Scherrer's formula, were determined to be 15.3 nm for undoped ZnO and 18.5 nm for sputtered AZO, further supporting structural differences.

While the examination of the film properties of as-deposited undoped ZnO film offers insights into its characteristics, its application as TCO layer in SHJ solar cells requires an additional annealing step when curing the screen-printed metallization, which may alter its properties. Consequently, we subjected the film to annealing under conditions analogous to the curing step in SHJ fabrication process with an annealing in ambient atmosphere in an oven at 170 °C for 40 min, with a focus on changes in its electrical properties. As shown in Table 2, the electrical properties of the undoped ZnO film deteriorated significantly postannealing. The charge carrier concentration decreased to 10^{18} cm^{-3} which could be attributed to the annealing process in air, during which oxygen species from the ambient can interact with the undoped ZnO film and modify electrically active donor states, including defect related to oxygen vacancies, as schematically shown in Figure 4 [10]. Crucially, the porous nature of the PECVD undoped ZnO likely exacerbates this effect by allowing oxygen to readily penetrate the grain boundaries and bulk through voids. At the same time, when the charge carrier concentration within a grain is low, the barrier height for carriers to move through grain boundaries becomes high, leading to reduced film mobility [38].

Overall, our study aligns with numerous previous reports indicating n-type conductivity in undoped ZnO film [27, 32, 39]. Several studies employing various types of CVD, such as low-pressure CVD, also report similar polycrystallinity with a pronounced diffraction peak (002) at deposition temperatures as low as 140 °C [27]. Although our PECVD undoped ZnO exhibits higher resistivities compared to the well-established sputtered AZO, its electrical properties surpass those reported in other CVD-based techniques [31, 40]. Typically, low resistivity (<10^{-3} Ω·cm) ZnO-based film is achieved through CVD at elevated deposition temperatures (>350 °C) with thickness ranging from 200 to 1200 nm [41]. However, our PECVD development, intended for use in SHJ solar cells, imposes constraints on deposition temperature and film thickness. Despite these limitations, our analysis of the optoelectrical properties and microstructure revealed that PECVD undoped ZnO remains suboptimal as a TCO layer in SHJ solar cells. Consequently, the primary focus of our ongoing film development efforts must be to enhance charge carrier mobility and improve film morphology to mitigate the harmful effects of porosity and thermal instability.

TABLE 2 | Charge carrier concentration, charge carrier mobility, and resistivity of PECVD undoped ZnO and sputtered AZO before and after annealing.

	n, 10^{20} cm^{-3}		μ, cm^2/Vs		ρ, 10^{-3} Ω·cm	
	ad	an	ad	an	ad	an
Undoped ZnO	1.5	0.09	2.3	0.6	16	1350
Sputter AZO	2.0	2.3	17.1	17.7	1.8	1.41

Abbreviation: an, annealed; ad, as-deposited.

2.2 | Application of Seed Layers

The previously developed suboptimal electrical and surface properties of PECVD undoped ZnO film necessitate a strategy to control the initial growth of film. To this end, we investigated the use of thin seed layers to template the subsequent deposition, an approach widely used to enhance the properties of ZnO-based material [42–44]. In this study, we employed sputtered AZO and sputtered ITO seed layers (each 13–15 nm thick), followed by the deposition of the undoped ZnO film ensuring total film thickness of ≈100 nm.

Hall measurements results demonstrate a significant enhancement in the electrical properties of the undoped ZnO film when deposited on seed layers, as shown in Figure 5. The films exhibited a decrease in resistivity, shifting from 10^{-2} Ω·cm range to 10^{-3} Ω·cm range. This improvement is directly attributed to a substantial increase in charge carrier mobility, which rises from 2.3 cm^2/Vs when deposited on bare glass to 18 cm^2/Vs for films deposited on seed AZO, and further to 24 cm^2/Vs for films grown on seed ITO. It is important to note that the mobility of the respective thin seed layers, AZO and ITO, is 8 and 25.7 cm^2/Vs, respectively. Because the mobility of the AZO-seeded film surpasses both the seed layer and the unseeded film, there is a strong evidence of the template effect. Here, the AZO and ITO seed layers optimize the nucleation and subsequent growth of ZnO, facilitating an improvement of microstructure and carrier transport within the bulk undoped ZnO layer. The lowest resistivity achieved was 1.4×10^{-3} Ω·cm, corresponding to an average sheet resistance of <150 Ω/sq, which is sufficient for a front-contact TCO layer in solar cell applications [45].

Crucially, the seeded TCO conferred more robust stability to the electrical properties postannealing in air. While the charge carrier concentration of as-deposited TCO was in similar range ($1.1–2.1 \times 10^{20}$ cm^{-3}), the postannealing behavior differed significantly. As previously discussed, annealing in air causes a dramatic reduction in n for the undoped ZnO film. In contrast, both AZO- and ITO-seeded layers maintained $n > 10^{20}$ cm^{-3} after annealing. This resilience confirms that the seed layers

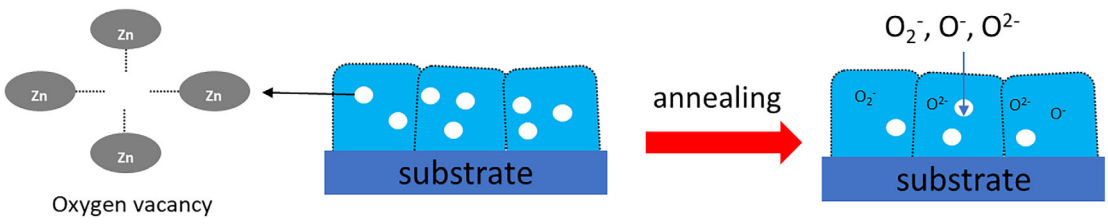


FIGURE 4 | Schematic illustration of annealing-induced changes in undoped ZnO thin films.

2367198x, 2026, 14, Downloaded from https://onlinelibrary.wiley.com/doi/10.1002/solr.70431 by Universitatsbibliothek RWTH Aachen University, Wiley Online Library on [03/08/2026]. See the Terms and Conditions (https://onlinelibrary.wiley.com/terms-and-conditions) on Wiley Online Library for rules of use; OA articles are governed by the applicable Creative Commons License

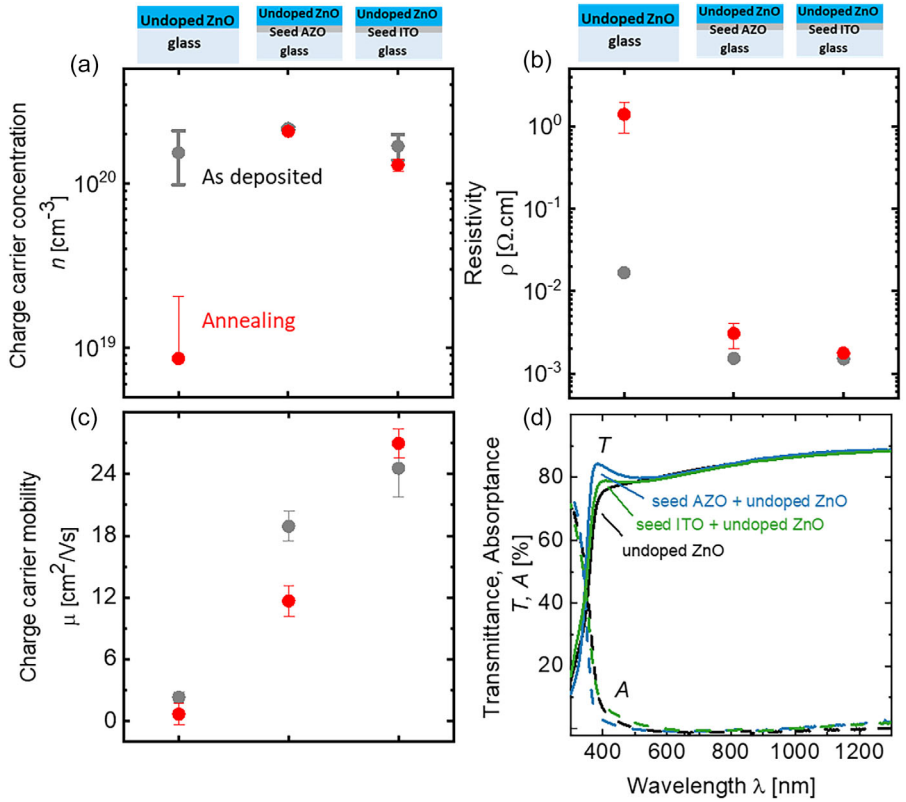


FIGURE 5 | Optoelectrical properties of undoped ZnO with seed layers. (a) Charge carrier concentration. (b) Resistivity. (c) Charge carrier mobility. (d) Transmittance and absorptance.

effectively promote a denser film structure, which likely hinders oxygen ingress and reduces the sensitivity of electrical performance to ambient-induced defect modification. Regarding optical properties, the seeded TCO films maintained high transmittance and low absorptance, as shown in Figure 5d. Although the data are presented in as-deposited films, the optical characteristics are representative as the annealed films demonstrate similar properties.

We hypothesized that the enhanced properties are rooted in the template effect of the seed layer, which governs the initial nucleation stage and subsequent film growth. In the PECVD process, DEZ and CO_2 were introduced into the reaction chamber. Under specific deposition temperatures and plasma conditions, DEZ molecules decompose, releasing Zn atoms, while CO_2 dissociates to form reactive oxygen species such as O atoms, O_2^-, or OH radicals [46, 47]. These Zn atoms and O species diffuse toward the substrate surface, resulting in the formation of ZnO. The reaction continued, facilitating the growth of the ZnO material. The seed layer acts as an energetically favorable template, promoting uniform adhesion and growth, which leads to a more dense material structure compared to the random nucleation and island formation observed on bare glass [47–49].

SEM top-view images of TCO with seed AZO (Figure 6a) reveal a fine and more uniform arrangement of spherical grains with no observable voids, unlike the unseeded film. It has been reported that deposition on a seed layer results in denser and more uniform particulates that interlink [48]. However, the ITO-seeded film displayed a leaf-like morphology with large grain features.

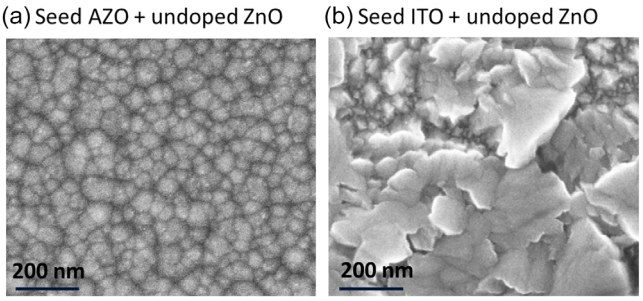


FIGURE 6 | SEM top-view images of PECVD undoped ZnO deposited on different seed layers. (a) ZnO grown on sputtered AZO seed layer. (b) ZnO grown on sputtered ITO seed layer.

It has been observed that multilayer TCO may have irregular surface, likely due to different orientations of seed layers affecting the growth of undoped ZnO film [50]. Overall, no observable voids are present in either film, which appears denser than the unseeded film. The refractive index for both seeded samples improved, as shown in Figure S2, confirming a high-quality, dense microstructure, which contrasts with the porous unseeded film. In addition, the contact angle measurements demonstrated a significant shift from hydrophilic behavior (54°–56°) to more hydrophobic properties (92°–93°) for the seeded films as shown in Figure S3.

GIXRD analysis shown in Figure 7 provided insight into the crystallographic evolution when different seed layers are applied. The seed AZO exhibited peaks at 34.4° and 62.9°, corresponding to

2367198x, 2026, 14, Downloaded from https://onlinelibrary.wiley.com/doi/10.1002/solr.70431 by Universitatsbibliothek RWTH Aachen University, Wiley Online Library on [03/08/2026]. See the Terms and Conditions (https://onlinelibrary.wiley.com/terms-and-conditions) on Wiley Online Library for rules of use; OA articles are governed by the applicable Creative Commons License

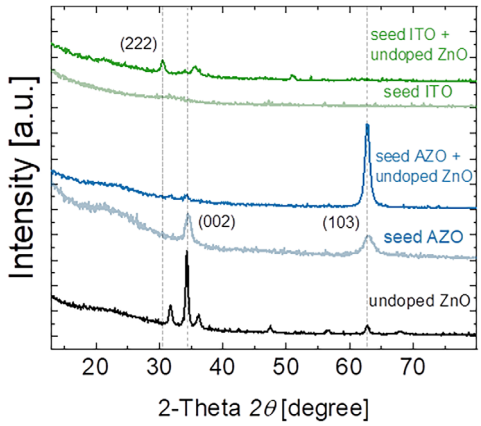


FIGURE 7 | XRD patterns of undoped ZnO deposited with and without seed layers. Diffraction patterns for the seed layers are given for the references.

the *c*-axis orientation (002) and (103) planes, respectively. Notably, the subsequent undoped ZnO layer exhibited a shift in the preferential orientation to the (103) plane (peak at 62.9°), with the (002) peak largely suppressed. In contrast, the thin seed ITO showed no visible peak, indicating an amorphous phase; however, diffraction peaks emerged in the film after the deposition of undoped ZnO. A small peak appeared at 30.5°, associated with a preferred orientation along (222) found in In_2O_3, according to JCPDS 06-0416 [43]. These peaks associated to different materials have been commonly reported in multilayer TCO [42, 43, 50, 51]. More intriguingly, the low intensity observed in our seed ITO suggests a low degree of crystallinity, which is consistent with other reports [43, 50].

The (103) peak in ZnO-based film has been attributed to various origins, one of which is the columnar growth crystalline grains forming cone-like crests [52]. Another origin is a superficial layer formed during deposition, where atoms diffuse more freely than those located deeper in the bulk; this layer is influenced by deposition temperature or the nature of substrate [37, 49]. Nonetheless, the direct impact of different crystalline phases on charge carrier mobility remains unclear, as only a few studies have addressed this issue. For instance, neither FWHM of (002) or (103) diffraction peaks nor their intensity ratio determined charge carrier mobility, but rather the surface morphology of film [49, 53]. Another study also concluded that their ZnO film could achieved high charge carrier mobility for films with varying crystalline phases [32].

In the analysis of the charge carrier mobility of TCO films, it is essential to consider factors such as crystallite size and scattering mechanisms [49]. Our GIXRD data did not indicate improved crystallinity or larger crystallite size; thus, the notable enhancement in charge carrier mobility in seeded TCO can be attributed to scattering mechanisms. Scattering from grain boundaries, optical phonons, and ionized impurities is the predominant mechanism that limits the transport of free electrons in degenerate TCO [28]. First, ionized impurity is primarily influenced by the charge associated with the formation of defect centers. As determined from Hall effect measurements, the charge carrier concentration in films was similar, we can infer a comparable number of defect centers or ionized free carrier. Second, lattice vibrations in TCO films are governed by temperature and give rise to phonons, which would be scattered with mobile electrons [54]. However, this is unlikely to be a factor since the Hall effect measurements were conducted under consistent conditions at room temperature. Assuming that ionized impurity and lattice vibrations effects are similar in our TCO films, the remaining grain boundary scattering emerges as a crucial factor in charge carrier mobility. In unseeded undoped ZnO with a porous film, numerous electron trap sites at the grain interfaces create a potential barrier that impedes carrier movement. Whereas in the seeded TCO, a denser film structure without observable voids can minimize scattering at grain interfaces and facilitating the free movement of charge carriers via thermionic emission over barriers and tunneling effects [55]. The increased mobility is thus a direct consequence of the reduction in grain boundary scattering due to the denser, more homogeneous microstructure templated by seed layers.

Overall, we demonstrated the benefits of employing seed layers to enhance the properties of PECVD undoped ZnO film. This approach not only improved the charge carrier mobility, thereby reducing resistivity, but also maintained its properties postannealing. Through this approach, we demonstrate the direct application of PECVD as a tool to deposit TCO layer in SHJ solar cells.

2.3 | Plasma-Enhanced Chemical Vapor Deposition ZnO as Transparent Conductive Layers in Silicon Heterojunction Solar Cells

This section presents the first direct application of our developed PECVD undoped ZnO film as a TCO layer in SHJ solar cells, utilizing the insights gained from the preceding thin-film characterization. Various TCO stacking configurations were employed on the front side of SHJ structure, as shown in Figure 8a. The resulting current–voltage (*I*–*V*) performance data, including open-circuit voltage V_{OC}, short-circuit current density J_{SC}, FF, pseudo fill factor (pFF), PCE η, and series resistance R_S, are shown in Figure 8b–f. Initial performance analysis revealed a noticeable drop in V_{OC} for structure 1 (unseeded undoped ZnO), which was 40–45 mV lower than that of the reference ITO-based cells, as shown by the dashed line in Figure 8b. This is an unexpected outcome, given that PECVD is generally regarded as a gentle deposition process that minimizes substrate damage [15]. The observed V_{OC} deficit suggests that the PECVD process, in its current state, adversely affects carrier selectivity or surface passivation layers. Quasisteady-state photoconductance (QSSPC) measurements were performed on *i*/*n* precursor stacks throughout the fabrication steps shown in Figure S4. While both sputtered ITO and PECVD ZnO induced an initial reduction in effective carrier lifetime, their recovery behaviors after annealing and light soaking differed significantly. Specifically, the PECVD ZnO sample exhibited negligible recovery, indicating that the deposition process caused permanent damage to the passivation stack. As this represents a novel approach to fabricate TCO layer, a comprehensive investigation is warranted to elucidate the mechanisms of damage during PECVD process and to optimize the process to mitigate these detrimental effects, which will be addressed in a separate study.

2367198x, 2026, 14, Downloaded from https://onlinelibrary.wiley.com/doi/10.1002/solr.70431 by Universitatsbibliothek RWTH Aachen University, Wiley Online Library on [03/08/2026]. See the Terms and Conditions (https://onlinelibrary.wiley.com/terms-and-conditions) on Wiley Online Library for rules of use; OA articles are governed by the applicable Creative Commons License

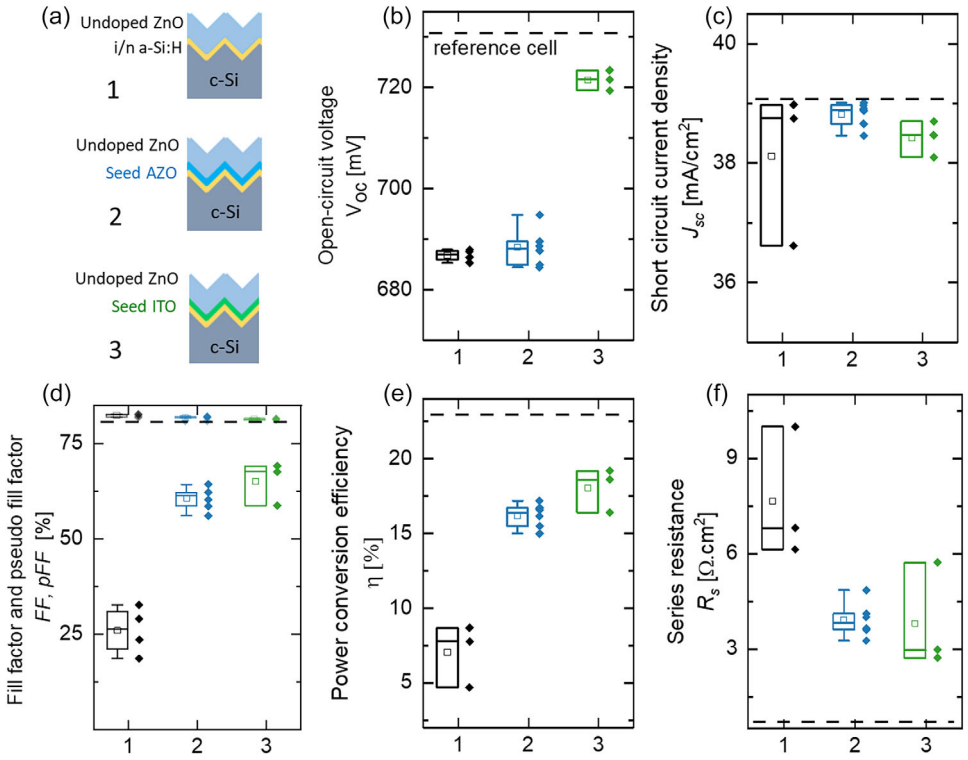


FIGURE 8 | Performance of SHJ solar cells with different front-side TCO stacks. (a) SHJ solar cell front side with different TCO layers, (b) open circuit voltage, (c) short-circuit current density, (d) FF and pFF, (e) PCE, (f) series resistance. The dashed line indicates the reference SHJ solar cells with sputtered ITO on both sides.

Structure 2 (AZO-seeded undoped ZnO) also exhibited a lower V_{OC}, consistent with our previous findings of sputter-induced damage during AZO deposition [42]. Notably, structure 3 (ITO-seeded undoped ZnO) achieved V_{OC} comparable to the reference cell. This finding suggests that a thin ITO seed layer not only templates the growth of the PECVD film but also serves as an effective buffer layer that minimizes permanent damage inflicted during the subsequent PECVD undoped ZnO process.

The excellent optical properties previously confirmed for the undoped ZnO film were effectively translated into device performance. Structures 1 and 2 demonstrated J_{SC} comparable to that of benchmark ITO-based SHJ solar cells, achieving J_{SC} >38.8 mA/cm^2, as shown in Figure 8c. A slightly reduced J_{SC} is observed in structure 3, possibly due to additional reflection at ITO/undoped ZnO interface and increased parasitic absorption. Despite the high J_{SC}, the average PCE for structure 1 was 7%, significantly lower than that of our reference cells with $\eta \approx 23.3\%$. The primary cause of this poor performance, in addition to the V_{OC} loss, was a low FF. The low FF in structure 1 is attributed to a significantly high R_S, which dragged the average FF down to ≈25% (Figure 8d). As previously discussed, the unseeded undoped ZnO film exhibited high film resistivity postannealing. Accordingly, the advantage of employing seed layers is clearly validated by the FF improvement. The average FF of structures 2 and 3 increased to 60.5% and 65.1%, respectively. The introduction of seed layers effectively reduced R_S in SHJ solar cells, confirming a direct correlation between film resistivity and device performance.

To gain further insights into R_S loss observed in solar cells, we evaluated the contact resistivity using transfer length method (TLM) from patterned structure of TCO/a-Si:H contact similar to our previous reports [8, 42]. As shown in Table 3, the unseeded undoped ZnO/a-Si:H interface exhibited a significantly higher contact resistivity compared to ITO reference structure, suggesting that the interface resistance is the dominant factor contributing to the large R_S in undoped ZnO-based SHJ cell. The strategy of employing a seed layer to improve contact was partially successful. While the ITO-seeded structure achieved ρc as low as 833 mΩ·cm^2, this value remains an order of magnitude higher than the reference cell. The origin of poor contact in undoped ZnO is likely due to band offset potential barrier and the intrinsic electronic properties of undoped ZnO film. First, the work function mismatches between n-type a-Si:H and TCO layers leads to the formation of Schottky barrier at the interface which hinders efficient carrier injection. While the work function of TCO can be adjusted by increasing carrier concentration, at the current stage, the introduction of dopants in our PECVD process is yet to be established [56]. To investigate this further, temperature-dependent Hall measurements in Figure S5 revealed a significant increase in film resistivity with temperature, accompanied by

TABLE 3 | Contact resistivity of TCO/a-Si:H.

TCO	Contact resistivity ρc, mΩ·cm^2
Undoped ZnO	18 147
Seed AZO + undoped ZnO	2471
Seed ITO + undoped ZnO	833
Reference ITO	87.5

2367198x, 2026, 14, Downloaded from https://onlinelibrary.wiley.com/doi/10.1002/solr.70431 by Universitatsbibliothek RWTH Aachen University, Wiley Online Library on [03/08/2026]. See the Terms and Conditions (https://onlinelibrary.wiley.com/terms-and-conditions) on Wiley Online Library for rules of use; OA articles are governed by the applicable Creative Commons License

simultaneous decrease in both charge carrier concentration and charge carrier mobility. This indicates that the carrier transport in undoped ZnO is governed by thermally activated potential barriers rather than degenerate tunneling. The depletion of carriers at elevated temperatures suggests that the depletion region at grain boundaries and TCO/a-Si:H interface is widened, causing a bottleneck for the charge transport.

Overall, our most efficient SHJ solar cells, featuring seed ITO/undoped ZnO film on the front side, exhibited V_{OC} of 723 mV, J_{SC} of 38.5 mA/cm^2, FF of 69.1%. These improvements are attributed to the reduced R_S resulting from lower contact resistivity compared to unseeded TCO. Consequently, a PCE of 19.2% was achieved. Despite the potential of PECVD-derived TCO, future work needs to focus on critical pathways, mitigating V_{OC} degradation caused by the PECVD process and introducing dopants into the film to improve the interface contact.

3 | Conclusion

In summary, we successfully developed a new route for preparing a TCO layer using the PECVD process of undoped ZnO thin films and investigated the film properties. The initial undoped ZnO film exhibited high resistivity and instability during air annealing, which was attributed to its porous nature. However, we demonstrated that utilizing AZO or ITO seed layers significantly mitigated these issues, resulting in a denser film with improved electrical properties. This work represents the first successful demonstration of employing PECVD-fabricated ZnO as a front TCO contact layer in SHJ solar cells. The feasibility of integrating PECVD process into SHJ solar cell fabrication was confirmed, and the advantages of using seed layers to improve film properties and consequently improve solar cell performance were proven. Despite the challenges regarding the initial film quality and the need to further optimize the PECVD conditions to maximize the device performance, this study provides valuable insights into the current limitations and opportunities of PECVD for TCO development. By focusing further research on refining the process and fully understanding the ideal deposition parameters, PECVD holds considerable potential to emerge as a viable alternative method for producing high-quality TCO with tunable properties for next-generation PV applications.

4 | Experimental Details

4.1 | Deposition and Characterizations of Transparent Conductive Oxide Films

Undoped ZnO films were deposited via PECVD process using a custom-built Von Ardenne system. Diethylzinc (DEZ, $(C_2H_5)_2Zn$) and carbon dioxide (CO_2) were used as precursors for zinc and oxygen, respectively. DEZ was stored in a steel cylinder maintained at 35 °C. DEZ was introduced into the deposition chamber using a bubbler system carried by Argon (Ar) gas. CO_2 and Ar gas flow rates were controlled using mass flow controllers. We set the baseline deposition process under the following conditions: substrate temperature of 200 °C, deposition pressure of 10 Pa, RF plasma mode at 100 W power, CO_2 flow at 8 sccm. The deposition was controlled to achieve a film thickness of 100 nm. This baseline process allows us to obtain a film with high transmittance and reasonable resistivity for SHJ applications. In addition, thin films (13–15 nm) of AZO and ITO were prepared using magnetron sputtering technique as previously reported in our studies [42].

In this study, TCO films were deposited on glass substrates (Corning Eagle 2000). Spectroscopic ellipsometry (J.A Woollam Model M2000) was used to determined film thickness and to obtained refractive index and Maxwell–Garnett EMA. The optical properties, such as transmittance and reflectance spectra, were measured in the range from 300 to 1300 nm using a ultraviolet–visible–near-infrared (UV–Vis–NIR) spectrophotometer (Lambda 950, Perkin Elmer). Additionally, charge carrier mobility, charge carrier concentration, and film resistivity were measured by Hall effect measurements with Van Der Pauw configuration at room temperature using an in-house built setup. For microstructural analysis, X-ray diffraction (XRD) patterns were obtained using a Bruker D8 Advance diffractometer setup in the grazing incidence XRD mode, while thickness and density of the films were determined in XRR setup at the same diffractometer. The surface morphology was observed using a scanning electron microscope (Zeiss 1550 VP) and surface roughness and morphology were evaluated by AFM, using a FlexAFM by Nanosurf [57]. The contact angle was measured using a Krüss Scientific instrument.

4.2 | Fabrication of Silicon Heterojunction Solar Cells

To fabricate SHJ solar cells, n-type Czochralski silicon wafers <100> from LONGi with a thickness of 135 µm and a resistivity of 1 Ω·cm were used. For each TCO stack, at least two SHJ devices were prepared. Each device consisted of four small subcells (19 × 19 mm^2) fabricated on the same quarter of a M2+ wafer (78 × 78 mm), as shown in Figure S6. The silicon substrates were cleaned and etched to texture both surfaces. Intrinsic and doped (p- and n-type a-Si:H) amorphous silicon films were prepared by PECVD, covering both sides. Subsequently, the rear ITO film ($In_2O_3/SnO_2 = 97/3$) was deposited via magnetron DC sputtering. Different TCO stacks were applied to the front side, consisting of PECVD undoped ZnO, thin AZO, and ITO, followed by PECVD undoped ZnO. Subsequently, silver electrodes were fabricated on both sides using a screen-printing process, followed by an annealing step at 170 °C for 40 min in an oven. Details of process steps to fabricate SHJ solar cells could be found elsewhere [58, 59]. Light soaking treatment was applied to the solar cells using GSOLA GLR-4Z [60]. Sinton WCT-120 utilizing QSSPC and transient photoconductance decay was used to measure the effective carrier lifetime of samples. The *I–V* performance data were evaluated using a solar simulator LOANA system from PV tools equipped with a Wavelab Sinus 220 light source under standard simulated AM 1.5G sunlight irradiance (100 mW/cm^2, 25 °C), where V_{OC}, J_{SC}, FF, pFF, η, and R_S were recorded. The PV parameters reported in this work correspond to measurements performed on the individual subcells. The reported values represent the mean value across the measured subcells, and the associated uncertainty corresponds to the standard deviation. TLM was used to determine contact

2367198x, 2026, 14, Downloaded from https://onlinelibrary.wiley.com/doi/10.1002/solr.70431 by Universitatsbibliothek RWTH Aachen University, Wiley Online Library on [03/08/2026]. See the Terms and Conditions (https://onlinelibrary.wiley.com/terms-and-conditions) on Wiley Online Library for rules of use; OA articles are governed by the applicable Creative Commons License

resistivity between TCO/a-Si:H. The TLM pattern was fabricated on the same wafer besides the subcells, consisting of eight rectangular pads with length 0.2 cm and width 1 cm and a spacing range from 0.5 to 11 cm, as shown in Figure S6. The contact resistivity was determined by measuring the J–V between adjacent pads under dark conditions and then extrapolating a linear behavior.

Acknowledgments

The authors would like to thank B. Zwaygardt, A. Doumit, H. Siekmann, V. Lauterbach, A. Mück, S. Lynen, H. Gattermann, A. Schmalen, and J. Wolff for their support and technical assistance. This work was supported by the Helmholtz Nano Facility funded by the Helmholtz Association. The authors would like to thank the Institute of Energy Technologies—Electrochemical Process Engineering (IET-4) for providing the contact angle instrument. This work was supported by the German Federal Ministry of Economic Affairs and Energy in the framework of the TOP project under the grant number 03EE1080B and SiLEAN project funded by the European Union under grant number 101147275. Views and opinions expressed are, however, those of the authors only and do not necessarily reflect those of the European Union. Neither the European Union nor the granting authority can be held responsible for them. Alexandros Sarantopoulos acknowledges for funding by Federal Ministry of Education and Research (project NEUROTEC, grant numbers 16ME0398K and 16ME0399). Muhammad Ainul Yaqin acknowledges the HITEC fellowship program for funding.

Open Access funding enabled and organized by Projekt DEAL.

Funding

This work was supported by the German Federal Ministry of Economic Affairs and Energy in the framework of the TOP project under the grant number 03EE1080B; SiLEAN project funded by the European Union under grant number 101147275; Federal Ministry of Education and Research, project NEUROTEC, grant numbers 16ME0398K and 16ME0399.

Conflicts of Interest

The authors declare no conflicts of interest.

Data Availability Statement

The data that support the findings of this study are available from the corresponding author upon reasonable request.

References

1. C. Ballif, F.-J. Haug, M. Boccard, P. J. Verlinden, and G. Hahn, "Status and Perspectives of Crystalline Silicon Photovoltaics in Research and Industry," *Nature Reviews. Materials* 7 (2022): 597–616.

2. B. Liang, X. Chen, X. Wang, et al., "Progress in Crystalline Silicon Heterojunction Solar Cells," *Journal of Materials Chemistry A* 13 (2025): 2441–2477.

3. H. Lin, M. Yang, X. Ru, et al., "Silicon Heterojunction Solar Cells with up to 26.81% Efficiency Achieved by Electrically Optimized Nanocrystalline-Silicon Hole Contact Layers," *Nature Energy* 8 (2023): 789–799.

4. Y. Li, X. Ru, M. Yang, et al., "Flexible Silicon Solar Cells with High Power-to-Weight Ratios," *Nature* 626 (2024): 105–110.

5. J. Haschke, O. Dupré, M. Boccard, and C. Ballif, "Silicon Heterojunction Solar Cells: Recent Technological Development and Practical Aspects - From Lab to Industry," *Solar Energy Materials and Solar Cells* 187 (2018): 140–153.

6. U. Chime, L. Wolf, V. Buga, et al., "How Thin Practical Silicon Heterojunction Solar Cells Could Be? Experimental Study under 1 Sun and under Indoor Illumination," *Solar RRL* 6 (2022): 2100594.

7. D. Qiu, W. Duan, A. Lambertz, et al., "Effect of Oxygen and Hydrogen Flow Ratio on Indium Tin Oxide Films in Rear-Junction Silicon Heterojunction Solar Cells," *Solar Energy* 231 (2022): 578–585.

8. Z. Yao, W. Duan, P. Steuter, et al., "Influence of Oxygen on Sputtered Titanium-Doped Indium Oxide Thin Films and Their Application in Silicon Heterojunction Solar Cells," *Solar RRL* 5 (2021): 2000501.

9. W. Cui, F. Chen, Y. Li, X. Su, and B. Sun, "Status and Perspectives of Transparent Conductive Oxide Films for Silicon Heterojunction Solar Cells," *Materials Today Nano* 22 (2023): 100329.

10. H. Liu, Y. Zhu, W. Xiong, Y. Yang, S. Li, and S. Bai, "Transparent Conductive Oxide Films and Their Applications in Silicon Heterojunction and Perovskite/Silicon Tandem Photovoltaics," *ACS Applied Energy Materials* 8 (2025): 4032–4047.

11. B. Demaurex, J. P. Seif, S. Smit, et al., "Atomic-Layer-Deposited Transparent Electrodes for Silicon Heterojunction Solar Cells," *IEEE Journal of Photovoltaics* 4 (2014): 1387–1396.

12. Y. Kuang, B. Macco, B. Karasulu, et al., "Towards the Implementation of Atomic Layer Deposited In2O3: H in Silicon Heterojunction *Solar Cells*," *Solar Energy Materials and Solar Cells* 163 (2017): 43–50.

13. T. Koida, T. Matsui, and H. Sai, "Amorphous SnO2 as Earth-Abundant Stable Transparent Conductive Oxide and Its Application to Si Heterojunction Solar Cells," *Solar RRL* 7 (2023): 2300381.

14. L. Barraud, Z. C. Holman, N. Badel, et al., "Hydrogen-Doped Indium Oxide/Indium Tin Oxide Bilayers for High-Efficiency Silicon Heterojunction *Solar Cells*," *Solar Energy Materials and Solar Cells* 115 (2013): 151–156.

15. E. Aydin, C. Altinkaya, Y. Smirnov, et al., "Sputtered Transparent Electrodes for Optoelectronic Devices," *Induced Damage and Mitigation Strategies. Matter* 4 (2021): 3549–3584.

16. M. Morales-Masis, S. De Wolf, R. Woods-Robinson, J. W. Ager, and C. Ballif, "Transparent Electrodes for Efficient Optoelectronics," *Advanced Electronic Materials* 3 (2017): 1600529.

17. X. Huang, Y. Zhou, W. Guo, et al., "Zr-Doped Indium Oxide Films for Silicon Heterojunction Solar Cells," *Solar Energy Materials and Solar Cells* 260 (2023): 112480.

18. J. Haschke, R. Lemerle, B. Aïssa, et al., "Annealing of Silicon Heterojunction Solar Cells: Interplay of Solar Cell and Indium Tin Oxide Properties," *IEEE Journal of Photovoltaics* 9 (2019): 1202–1207.

19. Y. Zhang, M. Kim, L. Wang, P. Verlinden, and B. Hallam, "Design Considerations for Multi-Terawatt Scale Manufacturing of Existing and Future Photovoltaic Technologies: Challenges and Opportunities Related to Silver{,} Indium and Bismuth Consumption," *Energy & Environmental Science* 14 (2021): 5587–5610.

20. A. B. Morales-Vilches, A. Cruz, S. Pingel, et al., "ITO-Free Silicon Heterojunction Solar Cells With ZnO: Al/SiO2 Front Electrodes Reaching a Conversion Efficiency of 23%," *IEEE Journal of Photovoltaics* 9 (2019): 34–39.

21. Z. Wu, W. Duan, A. Lambertz, et al., "Low-Resistivity p-Type a-Si: H/AZO Hole Contact in High-Efficiency Silicon Heterojunction Solar Cells," *Applied Surface Science* 542 (2021): 148749.

22. J. Wang, C. Meng, H. Liu, et al., "Application of Indium Tin Oxide/Aluminum-Doped Zinc Oxide Transparent Conductive Oxide Stack Films in Silicon Heterojunction Solar Cells," *ACS Applied Energy Materials* 4 (2021): 13586–13592.

23. K. Ellmer, A. Klein, and B. Rech, "ZnO and Its Applications," in *Transparent Conductive Zinc Oxide: Basics and Applications in Thin Film Solar Cells*, Vol. 104 (Springer, 2008), ISBN 978-3-540-73611-0.

2367198x, 2026, 14, Downloaded from https://onlinelibrary.wiley.com/doi/10.1002/solr.70431 by Universitatsbibliothek RWTH Aachen University, Wiley Online Library on [03/08/2026]. See the Terms and Conditions (https://onlinelibrary.wiley.com/terms-and-conditions) on Wiley Online Library for rules of use; OA articles are governed by the applicable Creative Commons License

24. X. Chen, X. Wang, B. Liang, et al., "Transparent Conductive Gallium-Doped Zinc Oxide Thin Films Grown by Reactive Plasma Deposition for Silicon Heterojunction Solar Cells," *ACS Applied Electronic Materials* 6 (2024): 8488–8496.

25. A. Favier, D. Muñoz, S. Martín de Nicolás, and P.-J. Ribeyron, "Boron-Doped Zinc Oxide Layers Grown by Metal-Organic CVD for Silicon Heterojunction Solar Cells Applications," *Solar Energy Materials and Solar Cells* 95 (2011): 1057–1061.

26. A. Cruz, F. Ruske, A. Eljarrat, et al., "Influence of Silicon Layers on the Growth of ITO and AZO in Silicon Heterojunction Solar Cells," *IEEE Journal of Photovoltaics* 10 (2020): 703–709.

27. D. Kim, H. Kim, K. Jang, S. Park, K. Pillai, and J. Yi, "Electrical and Optical Properties of Low Pressure Chemical Vapor Deposited Al-Doped ZnO Transparent Conductive Oxide for Thin Film Solar Cell," *Journal of the Electrochemical Society* 158 (2011): D191.

28. K. Ellmer and R. Mientus, "Carrier Transport in Polycrystalline ITO and ZnO: Al II: The Influence of Grain Barriers and Boundaries," *Thin Solid Films* 516 (2008): 5829–5835.

29. S. Duarte-Cano, L. Torrecilla, F. Pérez-Zenteno, et al., "Transparent Conductive Aluminum-Zinc Oxide Layers Deposited by High Pressure Sputtering," *Applied Surface Science* 713 (2025): 164357.

30. L. Fanni, B. Delaup, B. Niesen, et al., "Tuning the Porosity of Zinc Oxide Electrodes: From Dense to Nanopillar Films," *Materials Research Express* 2 (2015): 075006.

31. M. D. Barankin, E. Gonzalez II, A. M. Ladwig, and R. F. Hicks, "Plasma-Enhanced Chemical Vapor Deposition of Zinc Oxide at Atmospheric Pressure and Low Temperature," *Solar Energy Materials and Solar Cells* 91 (2007): 924–930.

32. X. Zeng, X. Wen, X. Sun, W. Liao, and Y. Wen, "Boron-Doped Zinc Oxide Thin Films Grown by Metal Organic Chemical Vapor Deposition for Bifacial a-Si: H/c-Si Heterojunction Solar Cells," *Thin Solid Films* 605 (2016): 257–262.

33. K. Zhang, O. Mashkov, M. A. Yaqin, et al., "Damp-Heat–Induced Degradation of Lightweight Silicon Heterojunction Solar Modules With Different Transparent Conductive Oxide Layers," *Progress in Photovoltaics: Research and Applications* 33 (2025): 541–550.

34. D. Bekermann, A. Gasparotto, D. Barreca, et al., "Highly Oriented ZnO Nanorod Arrays by a Novel Plasma Chemical Vapor Deposition Process," *Crystal Growth & Design* 10 (2010): 2011–2018.

35. C. Sanchez-Perez, S. C. Dixon, J. A. Darr, I. P. Parkin, and C. J. Carmalt, "Aerosol-Assisted Route to Low-E Transparent Conductive Gallium-Doped Zinc Oxide Coatings From Pre-Organized and Halogen-Free Precursor," *Chemical Science* 11 (2020): 4980–4990.

36. C. Charpentier, P. Prod\'homme, I. Maurin, M. Chaigneau, and P. Roca i Cabarrocas, "X-Ray Diffraction and Raman Spectroscopy for a Better Understanding of ZnO: Al Growth Process," *EPJ Photovoltaics* 2 (2011): 25002.

37. Y. Wang, X. Li, G. Jiang, W. Liu, and C. Zhu, "Origin of (103) Plane of ZnO Films Deposited by RF Magnetron Sputtering," *Journal of Materials Science: Materials in Electronics* 24 (2013): 3764–3767.

38. A. Wang, T. Chen, S. Lu, et al., "Effects of Doping and Annealing on Properties of ZnO Films Grown by Atomic Layer Deposition," *Nanoscale Research Letters* 10 (2015): 75.

39. A. Illiberi, F. Grob, C. Frijters, et al., "High Rate (∼7 Nm/s), Atmospheric Pressure Deposition of ZnO Front Electrode for Cu(In, Ga)Se2 Thin-Film Solar Cells with Efficiency beyond 15%," *Progress in Photovoltaics: Research and Applications* 21 (2013): 1559–1566.

40. M. E. Fragalà, G. Malandrino, M. M. Giangregorio, et al., "Optical, and Electrical Characterization of ZnO and Al-Doped ZnO Thin Films Deposited by MOCVD," *Chemical Vapor Deposition* 15 (2009): 327–333.

41. A. Illiberi, P. Poodt, P.-J. Bolt, and F. Roozeboom, "Recent Advances in Atmospheric Vapor-Phase Deposition of Transparent and Conductive Zinc Oxide," *Chemical Vapor Deposition* 20 (2014): 234–242.

42. Q. Tang, W. Duan, A. Lambertz, et al., ">85% Indium Reduction for High-Efficiency Silicon Heterojunction Solar Cells with Aluminum-Doped Zinc Oxide Contacts," *Solar Energy Materials and Solar Cells* 251 (2023): 112120.

43. Z. Yan, J. Shi, S. Chen, et al., "Gallium-Doped Zinc Oxide/Tungsten-Doped Indium Oxide Stacks with Enhanced Lateral Transport Capability for Efficient and Low-Cost Silicon Heterojunction Solar Cells," *Solar RRL* 8 (2024): 2301029.

44. S. Chen, J. Shi, Y. Yao, et al., "Tantalum-Doped Tin Oxide Rear Reflector for Efficient and Low-Cost Silicon Heterojunction Solar Cells," *Solar RRL* 9 (2025): 2400806.

45. A. Cruz, E.-C. Wang, A. B. Morales-Vilches, et al., "Effect of Front TCO on the Performance of Rear-Junction Silicon Heterojunction Solar Cells: Insights From Simulations and Experiments," *Solar Energy Materials and Solar Cells* 195 (2019): 339–345.

46. J. Sun, D. A. Mourey, D. Zhao, and T. N. ZnO. Jackson, "Thin Film, Device, and Circuit Fabrication Using Low-Temperature PECVD Processes," *Journal of Electronic Materials* 37 (2008): 755–759.

47. C.-H. Chao and D.-H. Wei, "Growth of Non-Polar ZnO Thin Films with Different Working Pressures by Plasma Enhanced Chemical Vapor Deposition," *Japanese Journal of Applied Physics* 53 (2014): 11RA05.

48. R. S. Kumar, P. Sudhagar, P. Matheswaran, R. Sathyamoorthy, and Y. S. Kang, "Influence of Seed Layer Treatment on ZnO Growth Morphology and Their Device Performance in Dye-Sensitized Solar Cells," *Materials Science and Engineering: B* 172 (2010): 283–288.

49. I. Cosme, S. Vázquez-y-Parraguirre, O. Malik, et al., "Differences between (103) and (002) X-Ray Diffraction Characteristics of Nanostructured AZO Films Deposited by RF Magnetron Sputtering," *Surface & Coatings Technology* 372 (2019): 442–450.

50. K.-L. Wang, Y.-Q. Xin, J.-F. Zhao, et al., "High Transmittance in IR Region of Conductive ITO/AZO Multilayers Deposited by RF Magnetron Sputtering," *Ceramics International* 44 (2018): 6769–6774.

51. P. Schmid, W. Wolke, H. Nagel, et al., "Reducing Indium Consumption in Silicon Hetero Junction Solar Cells With TCO Stack Systems of ITO and AZO," *IEEE Journal of Photovoltaics* 13 (2023): 646–655.

52. X. Li, Y. Wang, W. Liu, G. Jiang, and C. Zhu, "Study of Oxygen Vacancies' Influence on the Lattice Parameter in ZnO Thin Film," *Materials Letters* 85 (2012): 25–28.

53. G. Xiao-Yong, L. Qing-Geng, F. Hong-Liang, L. Yu-Fen, and L. Jing-Xiao, "Study on the Structural, Electrical, and Optical Properties of Aluminum-Doped Zinc Oxide Films by Direct Current Pulse Reactive Magnetron Sputtering," *Thin Solid Films* 517 (2009): 4684–4688.

54. K. Ellmer and R. Mientus, "Carrier Transport in Polycrystalline Transparent Conductive Oxides: A Comparative Study of Zinc Oxide and Indium Oxide," *Thin Solid Films* 516 (2008): 4620–4627.

55. J. H. Lee, Y. H. Kim, S. J. Ahn, T. H. Ha, and H. S. Kim, "Grain-Size Effect on the Electrical Properties of Nanocrystalline Indium Tin Oxide Thin Films," *Materials Science and Engineering: B* 199 (2015): 37–41.

56. H. Sai, T. Koida, and T. Matsui, "Improved Electrical Contact Properties in Indium-Free Silicon Heterojunction Solar Cells with Amorphous SnO2 TCO Layers," *Solar Energy Materials and Solar Cells* 278 (2024): 113191.

57. W. Albrecht, J. Moers, and B. Hermanns, "HNF-Helmholtz Nano Facility," *Journal of Large-Scale Research Facilities JLSRF* 3 (2017): A112–A112.

2367198x, 2026, 14, Downloaded from https://onlinelibrary.wiley.com/doi/10.1002/solr.70431 by Universitatsbibliothek RWTH Aachen University, Wiley Online Library on [03/08/2026]. See the Terms and Conditions (https://onlinelibrary.wiley.com/terms-and-conditions) on Wiley Online Library for rules of use; OA articles are governed by the applicable Creative Commons License

58. B. Xu, K. Bittkau, A. Eberst, et al., "Downshifting Encapsulant: Optical Simulation Evaluation of the Solution to Ultraviolet-Induced Degradation in Silicon Heterojunction Solar Cells," *Advanced Energy and Sustainability Research* 6 (2025): 2400227.

59. A. Eberst, B. Xu, K. Bittkau, A. Lambertz, U. Rau, and K. Ding, "Performance Improvements through Gradient Layers in Transparent Passivating Contact Solar Cells," *Cell Reports. Physical Science* 6 (2025): 102658.

60. W. Duan, T. Rudolph, H. T. Gebrewold, et al., "Insights into the Heat-Assisted Intensive Light-Soaking Effect on Silicon Heterojunction Solar Cells," *Solar RRL* 8 (2024): 2400383.

Supporting Information

Additional supporting information can be found online in the Supporting Information section.

2367198x, 2026, 14, Downloaded from https://onlinelibrary.wiley.com/doi/10.1002/solr.70431 by Universitatsbibliothek RWTH Aachen University, Wiley Online Library on [03/08/2026]. See the Terms and Conditions (https://onlinelibrary.wiley.com/terms-and-conditions) on Wiley Online Library for rules of use; OA articles are governed by the applicable Creative Commons License